



Co-Designed Reflective and Leaky-Waveguide Low-Pass Filter for Superconducting Circuits

Downloaded from: <https://research.chalmers.se>, 2026-03-04 21:52 UTC

Citation for the original published paper (version of record):

Andersson, L., Olsson, B., Gasparinetti, S. et al (2026). Co-Designed Reflective and Leaky-Waveguide Low-Pass Filter for Superconducting Circuits. *IEEE Transactions on Microwave Theory and Techniques*, 74(2): 1708-1714. <http://dx.doi.org/10.1109/TMTT.2025.3640205>

N.B. When citing this work, cite the original published paper.

© 2026 IEEE. Personal use of this material is permitted. Permission from IEEE must be obtained for all other uses, in any current or future media, including reprinting/republishing this material for advertising or promotional purposes, or reuse of any copyrighted component of this work in other works.

Co-Designed Reflective and Leaky-Waveguide Low-Pass Filter for Superconducting Circuits

Linus Andersson¹, Benjamin Olsson², Simone Gasparinetti³, and Robert Rehammar¹

Abstract—A stepped-impedance low-pass filter with integrated hollow waveguide absorbers is presented. The filter combines low insertion loss in the passband with strong attenuation at high frequencies, making it well suited for superconducting quantum computing applications, where qubits are sensitive to both near-band and far out-of-band radiation. The structure is implemented in a rectangular coaxial geometry, with inductive sections coupled to circular hollow waveguides oriented orthogonally to the transmission axis. Above their cutoff frequency, these waveguides efficiently couple to radiation inside the stepped-impedance filter, absorbing energy that would otherwise cause Cooper pair breaking in conventional superconductors. Optimal dimensions were obtained using a differential evolution (DE) algorithm applied to interpolated electromagnetic simulation data. A prototype was fabricated and characterized using a calibrated vector network analyzer (VNA) up to 67 GHz. Measurements confirm a 3-dB cutoff frequency at 13.7 GHz, insertion loss below 0.4 dB for frequencies under 8 GHz, and more than 48.5-dB rejection above 17.3 GHz. The design offers a compact, low-loss solution for near-band filtering and suppression of quasiparticle-generating radiation in cryogenic quantum systems.

Index Terms—Filter design, filter optimization, high-energy radiation drain (HERD) filter, infrared (IR) radiation, quantum computing, quasiparticles, simulation and modeling.

I. INTRODUCTION

SUPERCONDUCTING circuits are among the most promising building blocks for implementing fully functional quantum computers [1], [2]. Based on Josephson junctions [3], these devices, in combination with passive microwave circuitry, form highly nonlinear quantum circuits that can be operated as qubits. Superconducting qubits are highly sensitive to electromagnetic radiation both near and far from their operational frequency, typically in the 4–8-GHz range. To mitigate the detrimental effects of such radiation, the qubit input and output lines are commonly filtered using the

combinations of LC filters, absorptive filters, and cryogenic isolators.

Near-band, off-resonant electromagnetic interference has been shown to adversely affect the performance of superconducting qubits. The known mechanisms include ac Stark shifts of qubit frequencies [4], [5] and resonant excitation of higher order circuit modes, box modes of the circuit housing package [6], and spurious two-level systems and fluctuators in the vicinity of the qubits. To mitigate these effects, filters with sharp roll-off at the edge of the operational band are typically used.

Another source of decoherence comes into play at much higher frequencies. In a superconductor well below its critical temperature, T_C , the dominant charge carriers are Cooper pairs [7]. For frequencies above $2\Delta/\hbar$, where Δ is the superconducting energy gap and \hbar is the reduced Planck constant, radiation incident on the superconductor, typically above 80 GHz for aluminum thin films, can break the Cooper pairs, creating Bogoliubov quasiparticles [7]. These quasiparticles can degrade the qubit lifetime and coherence by tunneling through the Josephson junction [8], [9], [10]. Despite quasiparticle densities being experimentally observed to be several orders of magnitude larger than predicted [11], the presence of quasiparticles is not expected to limit qubit performance until coherence times approach the millisecond range [12]. As coherence times now start to reach such levels [13], [14], [15], careful strategies to mitigate quasiparticle effects have become increasingly important.

The reasons for the excess of quasiparticles are thermal radiation inside the cryogenic environment [16], [17], ionizing radiation, generating bursts of quasiparticle tunneling events [18], [19], [20], [21], [22], and phonon-only events related to stress in the substrate and thin films [23]. Mitigating sensitivity to ionizing impacts and phonon-only events are important, given their detrimental effects on quantum error correction [24]. Resilience to such events can be addressed through gap engineering of the junctions [25], [26], [27], [28] and phonon-trapping techniques [23], [29], [30].

Reducing quasiparticle tunneling caused by high-frequency radiation from the cryogenic environment can be achieved through light-tight packaging and shielding of the quantum processor [31], as well as by using infrared (IR) blocking filters on the input and output lines for a qubit. Usually, filters for this purpose are based on coaxial waveguides filled with absorptive materials [32], [33], [34], [35], [36]. Measurements have shown to significantly reduce the average quasiparticle

Received 4 August 2025; revised 13 October 2025; accepted 18 November 2025. Date of publication 23 December 2025; date of current version 6 February 2026. This work was supported by the Knut and Alice Wallenbergs Stiftelse (KAW) via the Wallenberg LaunchPad (WALP) Program. The work of Linus Andersson was supported by European Union under Grant 101135240 JOGATE. The work of Simone Gasparinetti was supported in part by European Research Council under Grant 101041744 ESQuAT and in part by the Knut and Alice Wallenberg foundation via the Wallenberg Centre for Quantum Technology (WACQT). The work of Robert Rehammar was supported by the Knut and Alice Wallenberg foundation via the WACQT. (Corresponding author: Linus Andersson.)

Linus Andersson, Simone Gasparinetti, and Robert Rehammar are with the Department of Microtechnology and Nanoscience, Chalmers University of Technology, 412 96 Göteborg, Sweden (e-mail: anlinus@chalmers.se).

Benjamin Olsson is with the Department of Information Technology, Uppsala University, 751 05 Uppsala, Sweden.

Digital Object Identifier 10.1109/TMTT.2025.3640205

tunneling rates, as demonstrated in [17], through improved light-tightness and extensive use of IR blocking filters.

While effective at absorbing high-frequency radiation, absorptive materials inside the waveguide also introduce unwanted loss at frequencies, where low insertion loss is critical. On readout lines, where quantum-noise-limited parametric amplifiers [37], [38] and cryogenic low-noise amplifiers [39], [40] are used, preserving signal level is crucial. Therefore, there is a clear need for filter technologies that overcomes the tradeoff of having low in-band loss while providing strong out-of-band absorption. On input lines that route control signals to the quantum processor, heavy attenuation is applied to thermalize room-temperature noise down to millikelvin temperatures [41]. Despite being heavily attenuated, maintaining a flat attenuation profile is also desired in order to avoid pulse distortions that can degrade qubit gate fidelity [42]. Traditional absorptive filters often fail in this regard, owing to their strong frequency-dependent loss.

Recently, a new absorptive low-pass filter type, termed the high-energy radiation drain (HERD), was demonstrated. This filter overcomes this tradeoff, exhibiting less than 0.15-dB insertion loss below 12 GHz while providing more than 60-dB absorption above 70 GHz, characterized up to 145 GHz [43]. Moreover, the HERD concept has been realized using multiple technological platforms, including a printed-circuit-board implementation that shows similar high-frequency suppression, demonstrating the broadband stopband of the HERD technique [44]. Since then, the HERD filter has been deployed in cryogenic systems achieving the state-of-the-art qubit readout [45], [46], high-saturation traveling-wave parametric amplification [47], and millisecond qubit coherence times [14]. Quasiparticle tunneling rates comparable to the best achieved with conventional absorptive filters have also been demonstrated [28]. However, a weakness of the conventional HERD design is its slow roll-off from passband to the highly attenuating stopband. Therefore, this filter is often combined with separate LC filter with lower cutoff frequency and sharper roll-off.

In this article, we report on investigations that extend this filtering approach by integrating the hollow waveguide structures into a stepped-impedance low-pass filter, achieving both high near-band rejection and strong absorption of Cooper pair-breaking frequencies well beyond the design reported in [43]. By optimizing the filter geometry, we achieve a 3-dB cutoff frequency at 13.5 GHz, an insertion loss of less than 0.45 dB below 8 GHz, and more than 52.7 dB of rejection above 17.3 GHz. This filtering technique eliminates the need for using combinations of LC and absorptive filters, reducing component overhead and enabling further scaling of quantum processors.

II. DESIGN

The stepped-impedance HERD low-pass filter is constructed from two computer numerical control (CNC)-machined copper blocks that, when soldered together, form the outer conductor of a rectangular coaxial transmission line. A flat copper strip serves as the center conductor. This configuration supports a transverse electromagnetic (TEM) mode, as well as higher

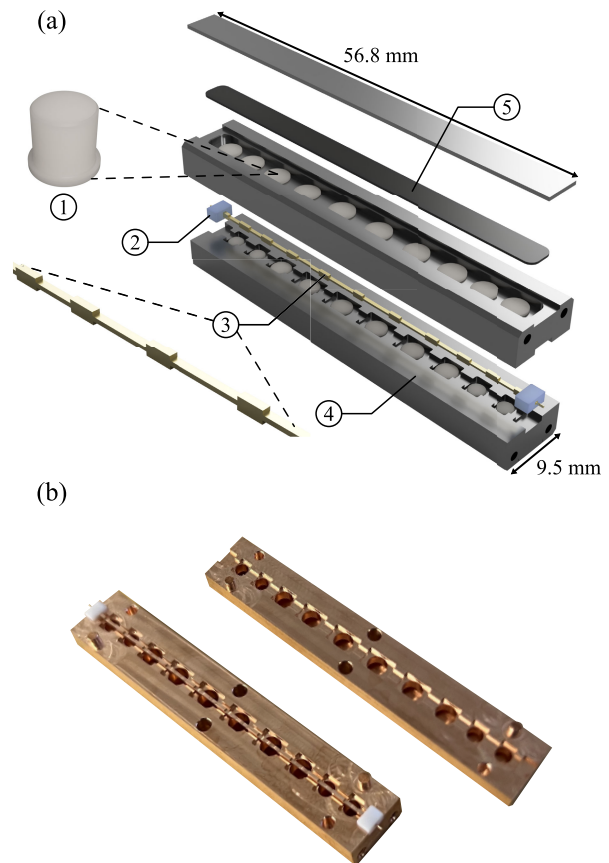


Fig. 1. (a) 3-D exploded view of the filter assembly (colored for visibility). The different parts of the assembly are indicated with numbers: 1) the MACOR ceramic slab, which are inserted into the HWs; 2) PTFE piece used to fixate the center conductor; 3) the center conductor, where the modulation of the conductor height can be seen; 4) outer conductor block with different sections of high and low impedance; and 5) absorptive foam to absorb the leaking radiation from the HWs. (b) Photograph of the outer conductor blocks with the central line fixated to one of the halves with pieces of PTFE.

order transverse electric (TE) and transverse magnetic (TM) modes. The center transmission line is coupled to circular HWs oriented perpendicularly out from the main waveguide's outer conductor (see [43] for a detailed discussion). The HWs have a cutoff frequency of approximately 25 GHz, well above the typical operating frequency of superconducting qubits (4–8 GHz). An exploded view of the filter assembly can be found in Fig. 1 together with the photographs of the manufactured prototype.

The filter comprises several sections of varying width and height for the inner and outer conductor. These variations create the sections of high or low impedance. In general, if a section of transmission line is short compared to the wavelength, it can be approximated as a reactive element. For a high-impedance section, the corresponding inductance is approximately

$$L = \frac{\beta \ell Z_h}{R_0} \quad (1)$$

while for a low-impedance section, the equivalent capacitance is

$$C = \frac{\beta \ell R_0}{Z_\ell} \quad (2)$$

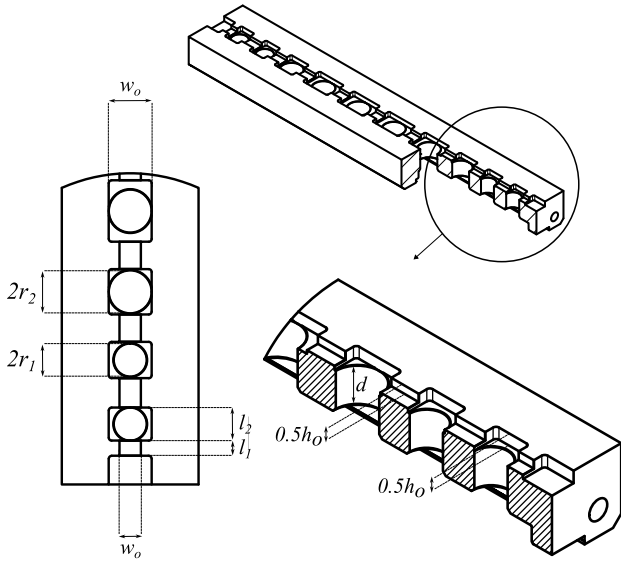


Fig. 2. Cross-sectional view of the outer conductor block with dimensions.

where β is the phase constant and ℓ is the physical length of the section [48]. The impedances Z_h and Z_ℓ are the characteristic impedance of the high- and low-impedance sections, respectively. R_0 is the system reference impedance.

In our implementation, the impedance is set by adjusting the outer conductor width w_o and height h_o , as well as the center conductor height h_i . The HWs are embedded in the high-impedance sections for two key reasons. First, their presence locally increases the inductance of the section due to partial field leakage and evanescent mode excitation near the waveguide apertures. Second, a larger outer cross section in the high-impedance regions permits full aperture exposure of the HWs, enhancing the electromagnetic coupling to out-of-band radiation. The HWs are symmetrically placed above and below the center conductor, coinciding with the regions of maximum TE field. A detailed view of the filter geometry can be seen in Fig. 2.

A. Dimensions and Material Choices

Achieving a high impedance contrast, Z_h/Z_ℓ , is critical to produce a sharp transition between passband and stopband. In the present prototype, the low-impedance sections have $Z_\ell = 22.1 \Omega$, while the high-impedance sections have $Z_h = 85.9 \Omega$.

The TEM mode profiles are simulated in COMSOL Multiphysics [49], where the characteristic impedance is calculated as

$$Z_0 = \frac{V}{I} = \frac{\int_\ell \vec{E}_t \cdot d\vec{\ell}}{\oint_C \vec{H}_t \cdot d\vec{\ell}} \quad (3)$$

where the numerator represents the line integral of the TE field between the conductors and the denominator the loop integral of the transverse magnetic field around the center conductor. The impedance varies along the HW-loaded inductive sections; we extract Z_0 at the axial midpoint, where the HW aperture is fully exposed.

TABLE I
FILTER GEOMETRY PARAMETERS

Parameter	Symbol	Value
Inner conductor height	h_i	0.8, 0.3 mm
Outer conductor width	w_o	1.5, 3 mm
Outer conductor height	h_o	1, 1.45 mm
HW radii	r_s, r_l	1.15, 1.5 mm
HW depth	d	2.5 mm
MACOR permittivity	ϵ_r	5.64
MACOR loss tangent	$\tan \delta$	2.5×10^{-3}

To reduce the cutoff frequency and thereby the physical size of the HWs, they are filled with the machinable glass ceramic MACOR. Two distinct slab radii, r_1 and r_2 , are used, which further suppresses the out-of-band retransmission of the stepped impedance filter by introducing poles at different frequencies. Sufficient depth d of the HWs is critical to prevent evanescent tunneling of the in-band modes. Below cutoff, the fields decay exponentially according to the expression

$$F(d) = e^{-\gamma d}, \quad \gamma = \sqrt{k_c^2 - k_0^2} \quad (4)$$

where k_c is the cutoff wavenumber and k_0 is the vacuum wavenumber. Away from the center conductor, the HWs are terminated with a carbon-loaded polyethylene foam to absorb radiated power. The foam is held in place with a piece of metal.

The center conductor is cut from a 0.5-mm copper sheet and slotted into a PTFE-filled 50- Ω TEM transmission section for alignment and mechanical stability. A summary of the geometrical parameters and material properties can be found in Table I.

B. Optimization Procedure

In order to reach the desired response of the LC filter, the lengths of each low and high impedance section need to be determined. For conventional, resonant filters, the optimal parameters can be synthesized from known polynomials [48]. As a result, only a final, local optimization of the physical geometry is usually needed to reach the desired response. However, for the filter prototype presented in this article, this approach was found to be inadequate. The filter comprises 21 sections, yielding a 21st-order stepped-impedance low-pass filter. Ten of those are the inductive sections, which embed the HWs. To account for the spatial variation of impedance within these sections caused by the presence of the HWs, as well as the complex field interactions at frequencies above cutoff, the inductive sections are modeled using COMSOL. This allows for accurate treatment of the geometry and electromagnetic response.

To optimize the length of the sections, we proceed as follows. First, we simulate the S -parameters of each inductive section as a function of physical length using frequency-domain finite element modeling (FEM) in COMSOL Multiphysics [49]. These results are then interpolated to obtain continuous S -parameter functions $S_{21}(f, \ell)$ and $S_{11}(f, \ell)$, seen in Fig. 3. From these results, their corresponding ABCD matrices are computed. The ABCD matrix for the

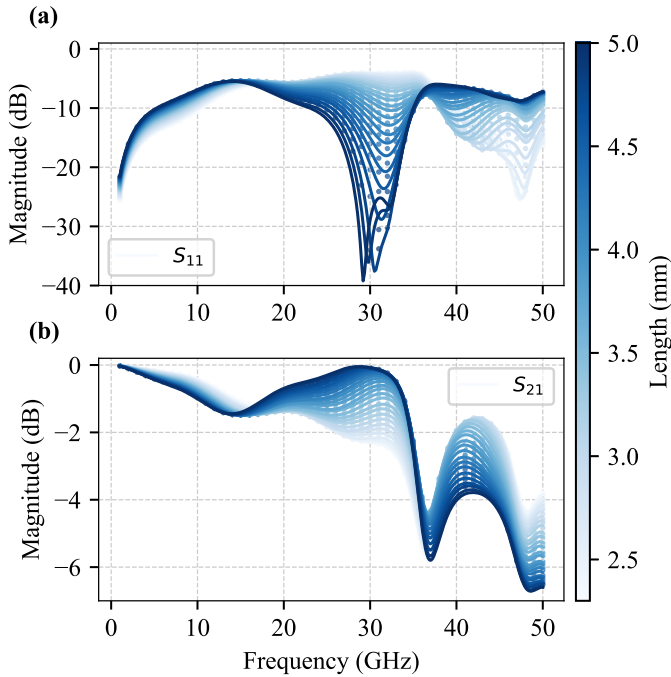


Fig. 3. Simulated (a) reflection coefficient S_{11} and (b) transmission coefficient S_{21} as functions of frequency for varying inductive section lengths. The length is swept from 2.5 to 5.0 mm, as indicated by the color scale.

capacitive sections is modeled using the standard transmission line theory

$$\mathbf{T}_i = \begin{bmatrix} \cos \beta \ell & jZ \sin \beta \ell \\ j\frac{1}{Z} \sin \beta \ell & \cos \beta \ell \end{bmatrix} \quad (5)$$

where the impedance comes from the mode analysis described above. To reduce the number of parameters in the optimization, the filter is made symmetric in the LC distribution; therefore, only 11 parameters need to be optimized. However, the central (11th) parameter corresponds to a capacitive section, which is split into two separate matrices in the calculation. The total filter response is obtained by cascading ABCD matrices according to

$$\mathbf{T}_{\text{tot}}(\omega; \ell) = \left(\prod_{i=1}^{N/2} T_i(\omega, \ell_i) \right) \left(\prod_{i=N/2}^1 T_i(\omega, \ell_i) \right) \quad (6)$$

where $N = 22$ and T_i is inductive when i is odd and capacitive when i is even.

To determine the optimal lengths, we use a differential evolution (DE) optimizer from the Python package SciPy [50], which is robust to local minima and does not require gradient information. The cost function penalizes passband ripple, insertion loss, and insufficient stopband attenuation. In this study, the optimization aimed for a return loss better than 20 dB below 12 GHz and an insertion loss greater than 50 dB in the 15–40-GHz range. As discussed in Section I, the superconducting qubits typically operate in the 4–8-GHz band. The 12-GHz cutoff was selected to also accommodate pump tones in the 10–12-GHz range, commonly used in driving parametric amplifiers for qubit readout. Additionally, we anticipate that the HW absorbers will dominate the stopband response above 40 GHz, which motivated choosing an upper frequency limit

TABLE II
OPTIMIZED SECTION LENGTHS OF
THE FILTER PROTOTYPE

Section	Length (mm)
1	1.06
2	2.30
3	2.05
4	2.54
5	1.91
6	3.16
7	1.91
8	4.28
9	1.77
10	4.63
11	0.80

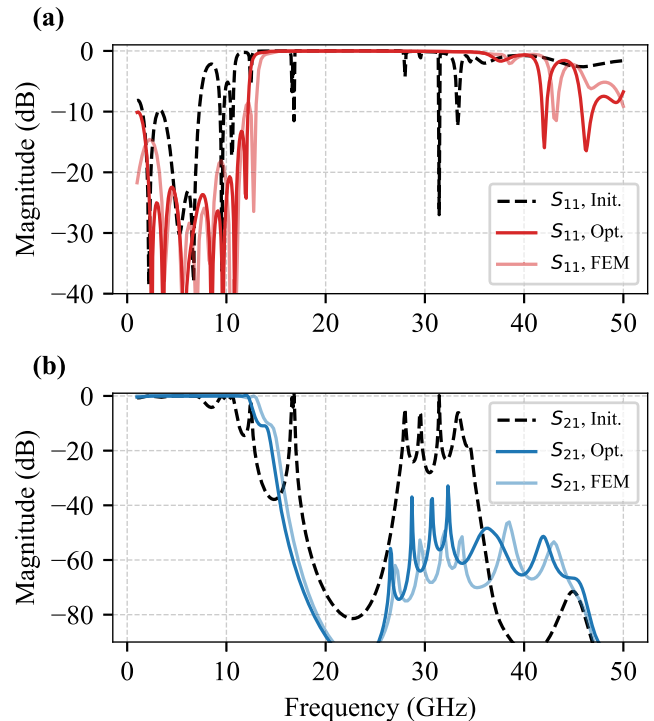


Fig. 4. Simulated (a) reflection coefficient, S_{11} and (b) transmission coefficient, S_{21} , showing the results of the filter geometry optimization. The dashed curves correspond to a randomly chosen initial parameter set. The solid curves represent the optimized solution, simulated either with the ABCD matrix model (darker shades of color) or with a full 3-D simulation (lighter shades). The observed shifts in response are attributed to 50- Ω PTFE sections, which are included in the FEM model but not in the ABCD-matrix optimization. The close agreement between the optimization results and full-wave simulations highlights the accuracy of the proposed design method.

of 40 GHz in the optimization. Once convergence is reached, the full 3-D model of the filter is simulated using FEM in COMSOL with all the optimized parameters to validate agreement with the simplified matrix-based model.

III. RESULTS

In this section, the results from the investigations of the full filter prototype are presented. The optimized parameters for the different sections can be found in Table II.

A. Optimized Filter

The optimization of the structure was performed using the method described in Section II-B. Starting from random

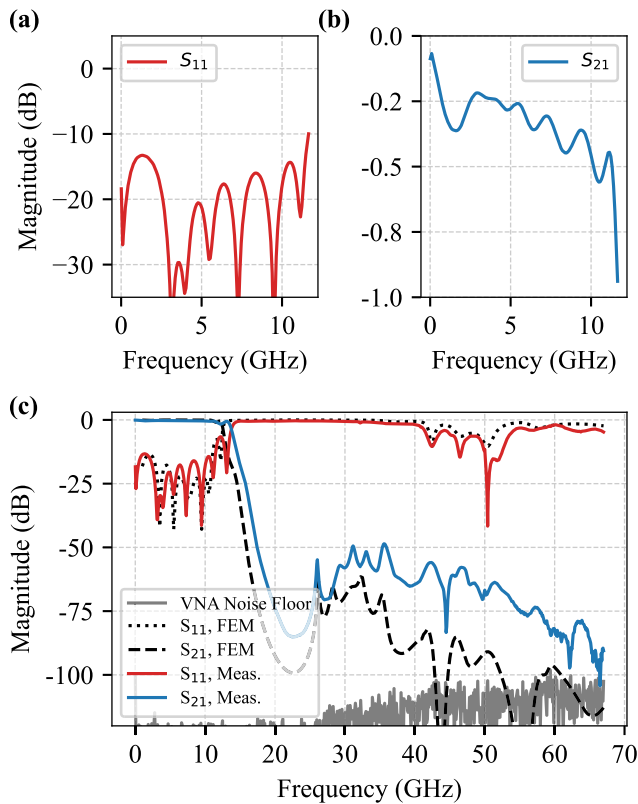


Fig. 5. Simulated and measured results for the final filter design. (a) and (b) Measured reflection coefficient S_{11} and transmission coefficient S_{21} in the passband, respectively. (c) Full-band response, comparing the measured data (red and blue solid) with full-wave FEM simulations (black dashed). The measured transmission closely follows the simulated response across the full frequency range. The light gray trace indicates the measured VNA noise floor. Minor deviations are attributed to connector transitions and modeling approximations outside the passband.

initial parameters, the optimizer converges to an acceptable solution, as shown by the simulated scattering parameters in Fig. 4. The return loss remains below -18 dB between 2.85–10.95 GHz, and the rejection in the stopband exceeds 50 dB above 15.85 GHz, close to the goals set in Section II-B. The results from the optimization are then verified using a full 3-D model of the complete filter. As seen, the ABCD-matrix model shows good agreement with the full 3-D EM simulation.

B. Measurements

The filter prototype was characterized using a Keysight PNA-X N5247B vector network analyzer (VNA), calibrated up to 67 GHz with an N4694A Electronic Calibration Module. To interface with the SMA connectors of the filter, Pasternack PE91619 1.85-/2.92-mm coaxial adapters were used in conjunction with Junkosha MWX261 1.85-mm cables. To resolve the stopband up to 67 GHz, an IF bandwidth of 10 Hz was used in combination with averaging. In order to further suppress the unwanted retransmission of the stepped-impedance filter, the apertures of the HWs on sections 6, 8, and 10 were increased from 2.3 to 3 mm in diameter. The measured S -parameters are presented in Fig. 5, along with simulated data obtained from a full-wave 3-D electromagnetic model of the structure.

Excellent agreement is observed between measurement and simulation across the whole passband, around the cutoff frequency, and at the onset of the stopband. Deviations above 30 GHz are attributed to limitations in the simulation model, in particular, the use of idealized scattering boundary conditions to terminate the hollow waveguide sections.

The VNA noise floor was determined by measuring the transmission while terminating the VNA ports with 50- Ω loads. This was done with the same calibration, IF bandwidth, and averaging as in the filter measurements. As shown in the plot, the measured stopband is resolved above the noise floor for the entire measurement bandwidth. The final prototype exhibits a 3-dB cutoff frequency at 13.7 GHz, an insertion loss below 0.4 dB for frequencies under 8 GHz, and a rejection exceeding 48.5 dB above 17.3 GHz, demonstrating the effectiveness of the optimized filter geometry.

IV. CONCLUSION

In this work, a compact stepped-impedance low-pass filter integrating hollow waveguide absorbers has been presented for suppressing high-frequency radiation in superconducting quantum processors. The design achieves a sharp passband-to-stopband transition with strong coupling to hollow waveguide terminations, which effectively absorb out-of-band radiation above the Cooper pair breaking frequencies of conventional superconducting thin films. By optimizing the filter dimensions using an ABCD-matrix-based approach guided by electromagnetic simulations, the prototype achieves a 3-dB cutoff at 13.7 GHz, an insertion loss below 0.4 dB for frequencies below 8 GHz, and rejection exceeding 48.5 dB above 17.3 GHz.

The filtering approach demonstrated here is general, and the underlying design principles can be adapted to different cutoff frequencies, depending on the available materials and fabrication processes. To design for other cutoff frequencies, changing the length of each section as well as the diameter of the hollow waveguides is required. We consider this filter to exhibit a Chebyshev-type response. Other filter responses may be possible with a different topology than stepped impedance. Further enhancement of stopband rejection may be possible by including the hollow waveguide diameter as an additional optimization parameter, potentially introducing more poles near the retransmission region of the stepped-impedance filter. This was not investigated in the present work due to added complexity in both optimization and fabrication.

These results highlight a compact filtering technique that combines multiple desirable properties well suited for the development of large-scale quantum computing architectures based on superconducting qubits. The proposed concept is also broadly applicable to superconducting circuits and other cryogenic or quantum systems, where low insertion loss and a wide stopband are critical.

The filter is patent pending.

ACKNOWLEDGMENT

The authors would like to thank Lars Jönsson for manufacturing the prototype. Linus Andersson, Simone Gasparinetti,

and Robert Rehammar are the co-founders and shareholders of Sweden Quantum AB. Other authors declare no competing interests.

REFERENCES

- [1] M. H. Devoret and R. J. Schoelkopf, "Superconducting circuits for quantum information: An outlook," *Science*, vol. 339, no. 6124, pp. 1169–1174, Mar. 2013. [Online]. Available: <https://www.science.org/doi/10.1126/science.1231930>
- [2] J. C. Bardin, D. Sank, O. Naaman, and E. Jeffrey, "Quantum computing: An introduction for microwave engineers," *IEEE Microw. Mag.*, vol. 21, no. 8, pp. 24–44, Aug. 2020. [Online]. Available: <https://ieeexplore.ieee.org/document/9134701>
- [3] T. V. Duzer and C. W. Turner, *Principles of Superconductive Devices and Circuits*, 2nd ed., Upper Saddle River, NJ, USA: Prentice-Hall, 1999.
- [4] D. I. Schuster et al., "AC stark shift and dephasing of a superconducting qubit strongly coupled to a cavity field," *Phys. Rev. Lett.*, vol. 94, no. 12, Mar. 2005, Art. no. 123602. [Online]. Available: <https://link.aps.org/doi/10.1103/PhysRevLett.94.123602>
- [5] A. Wallraff et al., "Approaching unit visibility for control of a superconducting qubit with dispersive readout," *Phys. Rev. Lett.*, vol. 95, no. 6, Aug. 2005, Art. no. 060501. [Online]. Available: <https://link.aps.org/doi/10.1103/PhysRevLett.95.060501>
- [6] S. Huang et al., "Microwave package design for superconducting quantum processors," *PRX Quantum*, vol. 2, no. 2, Apr. 2021, Art. no. 020306. [Online]. Available: <https://link.aps.org/doi/10.1103/PRXQuantum.2.020306>
- [7] M. Tinkham, *Introduction to Superconductivity*, 2nd ed., New York, NY, USA: Dover, 2004.
- [8] L. Glazman and G. Catelani, "Bogoliubov quasiparticles in superconducting qubits," *SciPost Phys. Lect. Notes*, p. 31, Jun. 2021. [Online]. Available: <https://scipost.org/10.21468/SciPostPhysLectNotes.31>
- [9] G. Catelani, R. J. Schoelkopf, M. H. Devoret, and L. I. Glazman, "Relaxation and frequency shifts induced by quasiparticles in superconducting qubits," *Phys. Rev. B, Condens. Matter*, vol. 84, no. 6, Aug. 2011, Art. no. 064517. [Online]. Available: <https://link.aps.org/doi/10.1103/PhysRevB.84.064517>
- [10] J. Aumentado, G. Catelani, and K. Serniak, "Quasiparticle poisoning in superconducting quantum computers," *Phys. Today*, vol. 76, no. 8, pp. 34–39, Aug. 2023, doi: [10.1063/pt.3.5291](https://doi.org/10.1063/pt.3.5291).
- [11] C. Wang et al., "Measurement and control of quasiparticle dynamics in a superconducting qubit," *Nature Commun.*, vol. 5, no. 1, p. 5836, Dec. 2014. [Online]. Available: <https://www.nature.com/articles/ncomms6836>
- [12] D. Ristè, C. C. Bultink, M. J. Tiggelman, R. N. Schouten, K. W. Lehnert, and L. DiCarlo, "Millisecond charge-parity fluctuations and induced decoherence in a superconducting transmon qubit," *Nature Commun.*, vol. 4, no. 1, p. 1913, May 2013. [Online]. Available: <https://www.nature.com/articles/ncomms2936>
- [13] A. Somoroff, Q. Ficheux, R. A. Mencia, H. Xiong, R. Kuzmin, and V. E. Manucharyan, "Millisecond coherence in a superconducting qubit," *Phys. Rev. Lett.*, vol. 130, no. 26, Jun. 2023, Art. no. 267001. [Online]. Available: <https://link.aps.org/doi/10.1103/PhysRevLett.130.267001>
- [14] M. P. Bland et al., "2D transmons with lifetimes and coherence times exceeding 1 millisecond," 2025, *arXiv:2503.14798*.
- [15] M. Tuokkola et al., "Methods to achieve near-millisecond energy relaxation and dephasing times for a superconducting transmon qubit," 2024, *arXiv:2407.18778*.
- [16] R. T. Gordon et al., "Environmental radiation impact on lifetimes and quasiparticle tunneling rates of fixed-frequency transmon qubits," *Appl. Phys. Lett.*, vol. 120, no. 7, Feb. 2022, Art. no. 074002, doi: [10.1063/5.0078785](https://doi.org/10.1063/5.0078785).
- [17] T. Connolly et al., "Coexistence of nonequilibrium density and equilibrium energy distribution of quasiparticles in a superconducting qubit," *Phys. Rev. Lett.*, vol. 132, no. 21, May 2024, Art. no. 217001. [Online]. Available: <https://link.aps.org/doi/10.1103/PhysRevLett.132.217001>
- [18] A. P. Vepsäläinen et al., "Impact of ionizing radiation on superconducting qubit coherence," *Nature*, vol. 584, no. 7822, pp. 551–556, Aug. 2020. [Online]. Available: <https://www.nature.com/articles/s41586-020-2619-8>
- [19] M. McEwen et al., "Resolving catastrophic error bursts from cosmic rays in large arrays of superconducting qubits," *Nature Phys.*, vol. 18, no. 1, pp. 107–111, Jan. 2022. [Online]. Available: <https://www.nature.com/articles/s41567-021-01432-8>
- [20] L. Cardani et al., "Reducing the impact of radioactivity on quantum circuits in a deep-underground facility," *Nature Commun.*, vol. 12, no. 1, p. 2733, May 2021. [Online]. Available: <https://www.nature.com/articles/s41467-021-23032-z>
- [21] P. M. Harrington et al., "Synchronous detection of cosmic rays and correlated errors in superconducting qubit arrays," 2024, *arXiv:2402.03208*.
- [22] C. D. Wilen et al., "Correlated charge noise and relaxation errors in superconducting qubits," *Nature*, vol. 594, no. 7863, pp. 369–373, Jun. 2021. [Online]. Available: <https://www.nature.com/articles/s41586-021-03557-5>
- [23] E. Yelton, C. P. Larson, K. Dodge, K. Okubo, and B. L. T. Plourde, "Correlated quasiparticle poisoning from phonon-only events in superconducting qubits," 2025, *arXiv:2503.09554*.
- [24] M. Mohseni et al., "How to build a quantum supercomputer: Scaling from hundreds to millions of qubits," 2024, *arXiv:2411.10406*.
- [25] M. McEwen et al., "Resisting high-energy impact events through gap engineering in superconducting qubit arrays," *Phys. Rev. Lett.*, vol. 133, no. 24, Dec. 2024, Art. no. 240601. [Online]. Available: <https://link.aps.org/doi/10.1103/PhysRevLett.133.240601>
- [26] J. M. Martinis, "Saving superconducting quantum processors from decay and correlated errors generated by gamma and cosmic rays," *NPJ Quantum Inf.*, vol. 7, no. 1, pp. 1–9, Jun. 2021. [Online]. Available: <https://www.nature.com/articles/s41534-021-00431-0>
- [27] J. Aumentado, M. W. Keller, J. M. Martinis, and M. H. Devoret, "Nonequilibrium quasiparticles and 2e periodicity in single-cooper-pair transistors," *Phys. Rev. Lett.*, vol. 92, no. 6, Feb. 2004, Art. no. 066802. [Online]. Available: <https://link.aps.org/doi/10.1103/PhysRevLett.92.066802>
- [28] H. Nho et al., "Recovery dynamics of a gap-engineered transmon after a quasiparticle burst," 2025, *arXiv:2505.08104*.
- [29] R.-P. Riwar et al., "Normal-metal quasiparticle traps for superconducting qubits," *Phys. Rev. B, Condens. Matter*, vol. 94, no. 10, Sep. 2016, Art. no. 104516. [Online]. Available: <https://link.aps.org/doi/10.1103/PhysRevB.94.104516>
- [30] U. Patel, I. V. Pechenezhskiy, B. L. T. Plourde, M. G. Vavilov, and R. McDermott, "Phonon-mediated quasiparticle poisoning of superconducting microwave resonators," *Phys. Rev. B, Condens. Matter*, vol. 96, no. 22, Dec. 2017, Art. no. 220501. [Online]. Available: <https://link.aps.org/doi/10.1103/PhysRevB.96.220501>
- [31] R. Barends et al., "Minimizing quasiparticle generation from stray infrared light in superconducting quantum circuits," *Appl. Phys. Lett.*, vol. 99, no. 11, Sep. 2011, Art. no. 113507, doi: [10.1063/1.3638063](https://doi.org/10.1063/1.3638063).
- [32] M. Halpern, H. P. Gush, E. Wishnow, and V. De Cosmo, "Far infrared transmission of dielectrics at cryogenic and room temperatures: Glass, fluorogold, eccosorb, stycast, and various plastics," *Appl. Opt.*, vol. 25, no. 4, pp. 565–570, Feb. 1986. [Online]. Available: <https://opg.optica.org/ao/abstract.cfm?uri=ao-25-4-565>
- [33] D. F. Santavicca and D. E. Prober, "Impedance-matched low-pass stripline filters," *Meas. Sci. Technol.*, vol. 19, no. 8, Jun. 2008, Art. no. 087001, doi: [10.1088/0957-0233/19/8/087001](https://doi.org/10.1088/0957-0233/19/8/087001).
- [34] A. Paquette et al., "Absorptive filters for quantum circuits: Efficient fabrication and cryogenic power handling," *Appl. Phys. Lett.*, vol. 121, no. 12, Sep. 2022, Art. no. 124001, doi: [10.1063/5.0114887](https://doi.org/10.1063/5.0114887).
- [35] J. M. Martinis, M. H. Devoret, and J. Clarke, "Experimental tests for the quantum behavior of a macroscopic degree of freedom: The phase difference across a Josephson junction," *Phys. Rev. B, Condens. Matter*, vol. 35, no. 10, pp. 4682–4698, Apr. 1987. [Online]. Available: <https://link.aps.org/doi/10.1103/PhysRevB.35.4682>
- [36] D. H. Slichter, O. Naaman, and I. Siddiqi, "Millikelvin thermal and electrical performance of lossy transmission line filters," *Appl. Phys. Lett.*, vol. 94, no. 19, May 2009, Art. no. 192508, doi: [10.1063/1.3133362](https://doi.org/10.1063/1.3133362).
- [37] A. Roy and M. Devoret, "Introduction to parametric amplification of quantum signals with Josephson circuits," *Comp. Rendus. Phys.*, vol. 17, no. 7, pp. 740–755, Aug. 2016. [Online]. Available: <https://www.sciencedirect.com/science/article/pii/S1631070516300640>
- [38] J. Aumentado, "Superconducting parametric amplifiers: The state of the art in Josephson parametric amplifiers," *IEEE Microw. Mag.*, vol. 21, no. 8, pp. 45–59, Aug. 2020. [Online]. Available: <https://ieeexplore.ieee.org/document/9134828>
- [39] M. W. Pospieszalski, "Extremely low-noise amplification with cryogenic FETs and HFETs: 1970–2004," *IEEE Microw. Mag.*, vol. 6, no. 3, pp. 62–75, Sep. 2005. [Online]. Available: <https://ieeexplore.ieee.org/document/1511915>
- [40] Y. Zeng, J. Stenarson, P. Sobis, N. Wadefalk, and J. Grahn, "Sub-mW cryogenic InP HEMT LNA for qubit readout," *IEEE Trans. Microw. Theory Techn.*, vol. 72, no. 3, pp. 1606–1617, Mar. 2024. [Online]. Available: <https://ieeexplore.ieee.org/document/10252156>

- [41] S. Krinner et al., "Engineering cryogenic setups for 100-qubit scale superconducting circuit systems," *EPJ Quantum Technol.*, vol. 6, no. 1, pp. 1–29, Dec. 2019. [Online]. Available: <https://epjquantumtechnology.springeropen.com/articles/10.1140/epjqt/s40507-019-0072-0>
- [42] S. Simbierowicz, V. Y. Monarkha, S. Singh, N. Messaoudi, P. Krantz, and R. E. Lake, "Microwave calibration of qubit drive line components at millikelvin temperatures," *Appl. Phys. Lett.*, vol. 120, no. 5, Feb. 2022, Art. no. 054004, doi: [10.1063/5.0081861](https://doi.org/10.1063/5.0081861).
- [43] R. Rehammar and S. Gasparinetti, "Low-pass filter with ultrawide stopband for quantum computing applications," *IEEE Trans. Microw. Theory Techn.*, vol. 71, no. 7, pp. 3075–3080, Jul. 2023. [Online]. Available: <https://ieeexplore.ieee.org/document/10032269/citations?tabFilter=papers#citations>
- [44] L. Andersson, "Miniaturized high-energy radiation drain filters for quantum computing applications," M.S. thesis, Dept. Microtechnology Nanoscience (MC2), Chalmers Univ. Technol., Gothenburg, Sweden, 2023. [Online]. Available: <https://hdl.handle.net/20.500.12380/306945>
- [45] P. D. Kurilovich et al., "High-frequency readout free from transmon multi-excitation resonances," 2025, *arXiv:2501.09161*.
- [46] S. Hazra et al., "Benchmarking the readout of a superconducting qubit for repeated measurements," *Phys. Rev. Lett.*, vol. 134, no. 10, Mar. 2025, Art. no. 100601. [Online]. Available: <https://link.aps.org/doi/10.1103/PhysRevLett.134.100601>
- [47] V. Gaydamachenko, C. Kissling, and L. Grünhaupt, "RF-SQUID-based traveling-wave parametric amplifier with input saturation power of -84 dBm across more than one octave in bandwidth," *Phys. Rev. Appl.*, vol. 23, no. 6, Jun. 2025, Art. no. 064053. [Online]. Available: <https://link.aps.org/doi/10.1103/1qk4-fzkq>
- [48] D. M. Pozar, *Microwave Engineering*. Hoboken, NJ, USA: Wiley, 2012.
- [49] (2025). *COMSOL Multiphysics*. [Online]. Available: <https://www.comsol.com>
- [50] P. Virtanen et al., "SciPy 1.0: Fundamental algorithms for scientific computing in Python," *Nat. Methods*, vol. 17, no. 3, pp. 261–272, 2020. [Online]. Available: <https://rdcu.be/b08Wh>



Benjamin Olsson received the B.Sc. degree in mathematics from the University of Florida, Gainesville, FL, USA, in 2022, and the M.Sc. degree in complex adaptive systems from the Chalmers University of Technology, Göteborg, Sweden, in 2025. He is currently pursuing the Ph.D. degree in machine learning at the University of Uppsala, Uppsala, Sweden.

He will apply mathematics and machine learning to oncology and microbial ecology at the University of Uppsala. His research is focused on the fields of machine learning, optimization, and applied mathematics.



Simone Gasparinetti received the Ph.D. degree in low-temperature nanophysics from Aalto University, Espoo, Finland, in December 2014.

After a Post-Doctoral appointment at ETH Zürich, Zürich, Switzerland, he moved to Chalmers University of Technology, Göteborg, Sweden, where he is currently an Associate Professor. His research group, the 202Q-lab, performs experiments on superconducting quantum circuits to address open questions in quantum information processing, quantum thermodynamics, and quantum-enabling technologies.



Linus Andersson received the M.Sc. degree in electrical engineering from the Chalmers University of Technology, Göteborg, Sweden, in 2023, where he is currently pursuing the Ph.D. degree in superconducting microwave electronics for quantum technologies.

His research interests include microwave circuits based on Josephson field-effect transistors (JOFETs), traveling-wave parametric amplifiers (TWPAs) based on nonlinear kinetic inductance, and the physics of quasiparticle generation in superconducting qubits.



Robert Rehammar received the M.Sc. degree in electrical engineering and the Ph.D. degree in applied physics from the Chalmers University of Technology, Göteborg, Sweden, in 2006 and 2012, respectively.

Between 2012 and 2021, he is in various positions in the industry working with applied microwave technology. Since 2021, he has been a Researcher at Chalmers University of Technology, Quantum Technology lab working on microwave quantum enabling solutions.